Omnidirectional Current Enhancement From Laminated Moth-Eye Textured Polymer Packaging for Large-Area, Flexible III-V Solar Modules

Gabriel Cossio, Evan D. Yu, Sudersena Rao Tatavarti, Brad Scandrett, and Edward T. Yu

Abstract—**Epitaxial lift-off (ELO) processes have allowed for cheaper development of mechanically flexible, ultra-thin, and high-efficiency III-V solar cells. ELO solar cells are natural candidates for applications where solar cells must conform to curved surfaces and provide high efficiency and high specific power generation (W/kg). Such examples include power generation for unmanned aerial vehicles, electric vehicles, and portable electrical power. However, when considering these mobile solar applications, large variations in angle of incidence (AOI) that inevitably occur can greatly decrease overall system efficiency due to significant Fresnel reflections. In this article, we demonstrate the integration of moth-eye antireflection nanostructures on the polymer packaging layer of ELO solar cell arrays using a low-cost, colloidal self-assembly process. The moth-eye structures mitigate Fresnel reflections and increase photocurrent generation over all measured angles of incidence relative to ELO solar cell arrays with traditional untextured polymer packaging. The nanostructures survive a commercial lamination procedure, an important criterion that must be met to ensure the feasibility of integration into commercial processing. Outdoor solar characterization measurements are performed and, under direct optical illumination, moth-eye textured solar cell arrays show a maximum I_{sc} enhancement of ∼58% at 79° AOI relative to traditional untextured polymer packaged solar cell arrays, and when exposed to both direct and diffuse optical illumination a maximum I_{sc} enhancement of ∼23% at 79° AOI is observed.**

Index Terms—**Antireflection, light management, multijunction solar cells, nanosphere lithography (NSL), nanostructures, omnidirectional, photovoltaic (PV) cells.**

I. INTRODUCTION

MECHANICALLY flexible solar cells have been proposed for a variety of applications for which traditional flat-plane photovoltaics (PV) are less suitable, including internet of things devices [1], [2], biological sensors [3]–[5], ultra-low-cost disposable power [6], [7], and general mobile power generation. Most effort has focused on development of solution processed organic or nanocrystalline PV technologies due to their low cost and the lower power requirements of their targeted applications. However, when considering applications that require high efficiency and large power outputs, the limited performance and stability of solution processed solar cells have limited their use.

Recently, high efficiency, lightweight, mechanically flexible epitaxial lift-off (ELO) [8]–[11] III-V solar cells have emerged as natural candidates to be used in mobile solar applications where higher power generation is required [12]–[15]. For example, new technologies such as high-altitude long endurance [16], [17] and low-altitude long endurance [18] unmanned aerial vehicles (UAVs) require efficient power generation and minimal addition to weight, making ELO solar cells a promising option. Similarly, mechanically flexible high-efficiency III-V solar cells have been investigated as power sources for next generation electric vehicles [19] as well as a potential solution to the critical problem of supplying power to forward military operating bases [12]. However, when considering mobile applications, large variations in angle of incidence (AOI) that inevitably occur can greatly decrease overall system efficiency due to significant Fresnel reflections [20], [21]. Last, to act as a truly mobile source of power, PVs must be able to provide reliable power generation under a wide range of illumination conditions. Previously, Trautz *et al.* [12] have shown that mobile solar power systems harvest 24% and 76% less energy on days with partial cloud and complete cloud cover when compared to a sunny day. Therefore, the reduced intensity and the large AOI range of diffuse optical illumination may become a significant limiting factor for overall device power conversion efficiency for mobile solar applications.

Previous studies have shown that employing advanced light management techniques can enable ultra-thin III-V solar cells to reach near optically thick efficiencies due to coherent light trapping [22]–[27]. However, the majority of studies have focused on optimizations for normal incidence illumination. Omnidirectional absorption enhancements, due to various combinations of

---

Manuscript received February 9, 2021; accepted February 28, 2021. Date of publication April 1, 2021; date of current version April 21, 2021. This work was supported in part by the University of Texas Microelectronics Research Center, a Member of the National Nanotechnology Coordinated Infrastructure; in part by the National Science Foundation under Grant ECCS-1542159, in part by the use of facilities and instrumentation supported by the National Science Foundation through the Center for Dynamics and Control of Materials: an NSF MRSEC under Cooperative Agreement DMR-1720595, in part by the Army Research Laboratory (Dr. Charles Rong), and in part by the National Science Foundation through the Industry/University Cooperative Research Center on Next Generation Photovoltaics (IIP-1540028 and IIP-1822206). *(Corresponding author: Edward T. Yu.)*

Gabriel Cossio and Edward T. Yu are with the Microelectronics Research Center, University of Texas at Austin, Austin, TX 78751 USA (e-mail: gcossio14@utexas.edu; ety@ece.utexas.edu).

Evan D. Yu is with the Westlake High School, Austin, TX 78746 USA (e-mail: yu.evan.d@gmail.com).

Sudersena Rao Tatavarti is with the Microlink Devices Inc., Niles, IL 60714 USA (e-mail: rtatavarti@mldevices.com).

Brad Scandrett is with the PowerFilm Solar Inc., Ames, IN 50014 USA (e-mail: bscan@powerfilmsolar.com).

Color versions of one or more figures in this article are available at https://doi.org/10.1109/JPHOTOV.2021.3065295.

Digital Object Identifier 10.1109/JPHOTOV.2021.3065295

2156-3381 © 2021 IEEE. Personal use is permitted, but republication/redistribution requires IEEE permission.
See https://www.ieee.org/publications/rights/index.html for more information.

Authorized licensed use limited to: University of Texas at Austin. Downloaded on June 25,2021 at 21:27:15 UTC from IEEE Xplore. Restrictions apply.

coherent light trapping and antireflective functionality, have also been demonstrated via surface texturing by wet etching [28]. However, antireflection structures fabricated via wet etching can suffer from increased surface and AUGER recombination that have limited their practical implementation [29]. Successful fabrication of an omnidirectional antireflection surface over large areas of a solar cell and at low cost would greatly benefit applications requiring mobile PV power generation.

Reflectance at the interface between air and dielectric packaging material for a solar module can also severely degrade power output of PV systems. One route to reduce surface reflectance and increase the power generation of a mobile PV power source is to transform the polymer packaging of a flexible ELO cell into an additional antireflective layer, thereby increasing the light reaching the solar cell absorber layer [30], [31]. We have shown in previous work [30] that nanotexturing the polymer packaging layer of smaller (1.1 cm^2) single junction GaAs solar cells increases J_{sc}, compared to that for cells with untextured polymer packaging, at all angles of incidence from 0° to 80°. Flexible ELO cells are often laminated between transparent polymer sheets to increase robustness and decrease environmental degradation. By adding "moth-eye" antireflection nanostructures [32]–[34] atop the polymer packaging layer, an additional omnidirectional antireflective surface can be integrated into the final PV device with minimal additional fabrication steps and without etching of the front semiconductor layer. By leveraging our previously reported large-area nanosphere lithography (NSL) technique, we are able to bypass the need for expensive lithography methods to fabricate the moth-eye nanostructures [35]. Similar processing techniques could be employed for fabrication of antireflective or light-trapping structures directly integrated with the actual solar cell device.

In this article, we demonstrate and characterize an eight cell, large area array of high efficiency, mechanically flexible triple junction (3J) solar cells with laminated moth-eye antireflection nanostructures fabricated using rapid, low-cost, scalable nanopatterning techniques. We show that the integration of an omnidirectional antireflective nanotextured surface into the polymer packaging layer of the flexible array of ELO solar cells greatly enhances the extraction of power from both the direct and the diffuse optical spectrum by reducing angle-dependent reflections compared to a PV device with an unpatterned packaging sheet. Low-cost, large-area NSL is employed to fabricate moth-eye antireflection nanostructures on a $\sim$200 cm^2 polyethylene terephthalate (PET) sheet used to encapsulate the array of high efficiency 3J ELO solar cells. Incorporating the antireflection moth-eye structures into the packaging layer of a PV array preserves the pristine crystal quality of the III-V absorber layers while still providing omnidirectional surface antireflection. We demonstrate that the nanotexturing survives a commercial lamination procedure while maintaining enhanced antireflection properties. Outdoor measurements show that solar cells with laminated moth-eye nanotextured PET have $\sim$9% and $\sim$58% higher I_{sc} (relative to that at normal incidence) than a non-nanotextured solar cell at 46° and 79° AOI, respectively, when under direct illumination. When under both diffuse and direct illumination, moth-eye patterned solar cells have a $\sim$6% and $\sim$23% enhancement in I_{sc} relative to untextured cells at 46° and 79°, respectively. The enhanced omnidirectionality of the PET integrated moth-eye nanostructures and the ability to leverage the power in the diffuse spectrum more efficiently could greatly benefit the long-term efficiency of PV systems and mobile power systems by providing the ability to generate more power under nonideal solar illumination conditions.

II. INVERTED METAMORPHIC MULTIJUNCTION DEVICE LAYER

All epitaxial structures were grown by metallorganic chemical vapor deposition at 100 mbar using arsine, phosphine, trimethylindium, and trimethylgallium as precursors and using a V/III ratio >50. Inverted metamorphic multijunction InGaP/GaAs/InGaAs structures were grown on GaAs substrates. The top InGaP cell has AlInP as the window layer and AlGaInP as the back-surface field (BSF) layer. The growth structure of the GaAs middle cell consisted of an InGaP window and BSF layers, an optically thick GaAs base layer doped with 2×10^{17} cm^{-3} p-type doping, and GaAs emitter with n-type doping in the range of 2×10^{18} cm^{-3}. The bottom 1.0 eV metamorphic cell was grown on top of an AlGaInAs graded buffer layer. The lattice constant of the buffer layer was graded from the GaAs middle cell value to that of $\text{In}_{0.31}\text{Ga}_{0.68}\text{As}$. The graded buffer layer was designed such that the smallest bandgap of the buffer layer was above the GaAs bandgap value of 1.42 eV.

III. EPITAXIAL LIFT-OFF (ELO) PROCESSING

The first layer deposited on the substrate is a thin AlGaAs release layer. The solar cell epitaxial layers are then deposited, followed by application of a thick (1–2 mil) flexible metal carrier layer. The wafer is then immersed in a concentrated HF-acid solution, which selectively dissolves the release layer (the etch selectivity relative to the GaAs epitaxial structure is greater than 1×10^5). The thin, composite structure consisting of the metal carrier layer and solar cell epitaxial layers is thereby completely separated from the GaAs substrate. The ELO process requires approximately 12 h to complete, but is amenable to batch processing, enabling scaling up of the process to lift off hundreds of substrates within a 24-h period.

IV. MULTISOLAR CELL ARRAY FABRICATION

After the ELO process and device fabrication, the wafers are diced into $\sim$20 cm^2 cells (6.7 × 3.1 cm each). All the contacts for the top and bottom side of the cell are made from the front side of the cell. Silver tabs are welded onto the top contact and we use solder to connect the bottom contact, which is the back of the cell. Cells are then interconnected in any desired fashion, in the present case in a 2 × 4 array configuration, where each set of four adjacent cells are wired in series with each other, and the two sets of series connected cells are wired in parallel. A back side adhesive layer with a polymer stiffener is placed on the build template for the array fabrication. Then a front side optically clear thermal polyurethane and the moth-eye textured sheets are placed on top of the cells and the whole stack is vacuum laminated. At the same time, fabric is placed behind the cells

Authorized licensed use limited to: University of Texas at Austin. Downloaded on June 25,2021 at 21:27:15 UTC from IEEE Xplore. Restrictions apply.

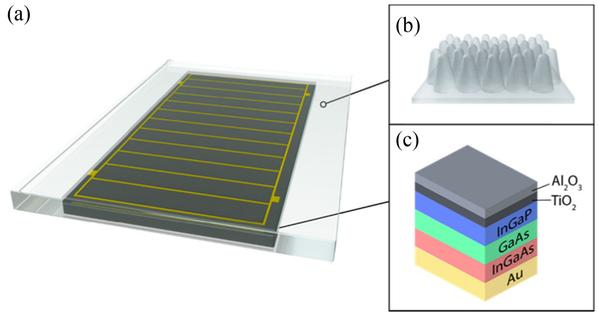

Fig. 1. (a) Schematic illustration of PET encapsulated triple junction ELO solar cell. (b) Schematic illustration of top surface of moth-eye textured PET encapsulant. (c) Schematic of triple junction ELO solar cell.

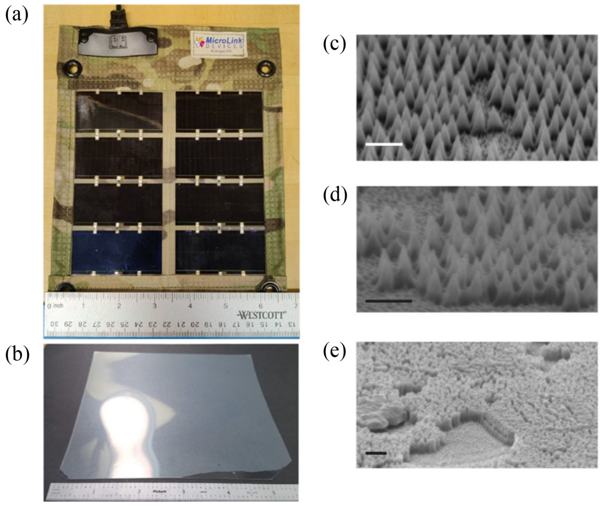

Fig. 2. (a) Eight cell 3J ELO solar cell array. (b) PET sheet coated with 200 nm polystyrene nanospheres used for fabrication of moth-eye nanostructures and lamination of the ELO array. The monolayer appears light blue–green in tint and covers the majority of the PET sheet. A defect can be seen in the bottom right corner of the PET sheet where the monolayer was not correctly transferred. From the defect, the transparent PET sheet can be seen in sharp contrast to the outline of the transferred nanosphere monolayer. (c) SEM image of PET moth-eye antireflection structures before lamination. Scale bar 400 nm (d) SEM image of PET moth-eye antireflection structures after optimized lamination. Scale bar 400 nm. (e) SEM image of PET moth-eye antireflection structures after standard nonoptimized lamination process. Scale bar 400 nm.

to complete the overall stack. After lamination the modules are tested for continuity, wired, sewn, labeled, and grommeted to form the final ruggedized package.

V. LAMINATED NANOTEXTURED PACKAGING SHEET FABRICATION

Moth-eye antireflection nanostructures are integrated into the top surface of a PET packaging layer atop a mechanically flexible ELO solar cell using a colloidal self-assembly process for nanopatterning followed by a dry etch. Fig. 1(a) shows a schematic illustration of the 3J solar cells used in this article. The solar cells are laminated between two 2 mil sheets of PET. Fig. 1(b) and (c) shows schematic illustrations of the moth-eye textured PET surface and the main layer structure of the solar cell, respectively. Eight 6.7 × 3.1 cm 3J ELO cells are used to create a final flexible array [Fig. 2(a)] which is encapsulated with a single large 5.5″ × 5.5″ nanotextured moth-eye PET sheet [Fig. 2(b)] via lamination. To fabricate the moth-eye structures, the PET is first coated with a monolayer array of hexagonally close packed 200 nm polystyrene (PS) nanospheres [Fig. 2(b)]. The 200 nm PS NS monolayer appears as a blue–green layer in Fig. 2(b). A patterning defect, which results in an unpatterned area of the PET sheet, can be seen at the bottom right corner of the PET sheet where the monolayer was not correctly transferred to the substrate.

A detailed description of the large-area NSL patterning process is presented elsewhere [35]. In brief, the NSs are injected onto the air–water interface of an aqueous reservoir where they self-assemble into a close packed array and are transferred to a PET sheet. After drying, the self-assembled monolayer and PET substrate are then simultaneously etched in a reactive ion etcher with an O_2 plasma. The simultaneous etching of the PS NSs and the polymer substrate forms the tapered moth-eye nanostructures. After etching of the moth-eye nanostructures, the ELO array is sandwiched between an untextured PET sheet (bottom side) and the moth-eye nanotextured PET (topside) with the, nanostructure facing the outside illumination source.

The lamination procedure involves placing a smooth ethylene–vinyl acetate coated release liner on top of the nanotextured surface. The sandwich is then subjected to 14 lb/in^2 and 135 °C for 3 min. Care must be taken during the lamination due to the low glass transition temperature of PET (70 °C). If either the pressure, temperature, or exposure time is too high, then irreversible degradation of the nanotextured surface can occur. Thermoplastic Polyurethane and Teflon release layers were also tested which resulted in worse degradation of the nanostructure. We found that lamination of the nanotextured polymer packaging sheet at 14 lb/in^2 and 135 °C for 3 min was able to make a robust seal and minimize the degradation of the nanostructure geometry. Unsuccessful lamination procedures allow the PET nanostructures to reflow and cause flattening of the nanostructure tips and neighboring nanostructures to fuse together as seen in Fig. 2(e). Fusing of the nanostructures can cause complete loss of antireflection properties since their antireflection behavior is in large part due to their tapered geometry. Using an optically clear polymer with a higher glass transition temperature, such as polycarbonate, may simplify the lamination of the polymer packaging sheet and minimize degradation of the nanostructures. Limited reflow of the PET is still present during successful lamination and leads to a slight loss in quality of the nanostructure geometry, as seen by the rougher texture and interconnected bases [Fig. 2(d)]. Scanning electron microscope images of PET moth-eye nanostructures before lamination are shown in Fig. 2(c). As will be shown, however, antireflection properties of the nanotextured packaging layer after lamination are maintained and show significant enhancement of I_{sc} at large AOI. The ability to successfully laminate the nanotextured PET sheet onto a flexible solar array is an important criterion that must

Authorized licensed use limited to: University of Texas at Austin. Downloaded on June 25,2021 at 21:27:15 UTC from IEEE Xplore. Restrictions apply.

be met to ensure the feasibility of integration into commercial processing.

VI. RESULTS AND DISCUSSION

Compared to a conventional single and double-layered thin film antireflection coating (DLARC), subwavelength nanostructures are able to maintain enhanced antireflection properties at very large AOI. The tapered geometry and subwavelength nature of the antireflection nanostructures (commonly referred to as moth-eye nanostructures in reference to their biomimetic origins [32]) allows for a gradual transition in the refractive index between two different optical media and reduces Fresnel reflections.

We have previously demonstrated fabrication of very large area (>200 cm^2) moth-eye textured PET sheets with an enhanced inexpensive NSL method [35]. Angle-dependent specular reflectance measurements were performed on both moth-eye textured and untextured sheets of PET to estimate the photon flux transmitted through the sheets [Fig. 3(a)]. Reflectance measurements were performed with a single grating monochromator (Optronics Laboratories OL-750 system). The photon fluxes shown in Fig. 3 are given by

$$\text{Photon Flux} \;=\; S\left(\lambda\right)\left(1-R\left(\lambda\right)\right)\frac{\lambda\left(\mu m\right)}{e*1.24} \qquad (1)$$

where $S(\lambda)$ is the AM1.5D [36] spectral irradiance in $\text{W/m}^2{*}\text{s}{*}\text{nm}$, $R(\lambda)$ is the measured reflectance spectrum, e is the electronic charge, and λ is the wavelength in micrometers. As can be seen from Fig. 3(a), the enhanced antireflection properties of the nanotextured PET sheets yield broadband increases in transmitted photon flux for both small AOI (30°) and larger AOI (70°). Fig. 3(b) shows the integrated photon flux through the PET sheets (black) and the ratio of transmitted photons through the moth-eye textured PET sheet relative to the untextured sheet (blue). Integrated photon flux was calculated by integrating (1) from 400 to 900 nm, the range of wavelengths for which $R(\lambda)$ was measured. For the 3J cells used in these studies, the integrated photon flux calculated using (1) provides an estimate of the total photon flux available for conversion to electric current by the 3J cells in the solar array.

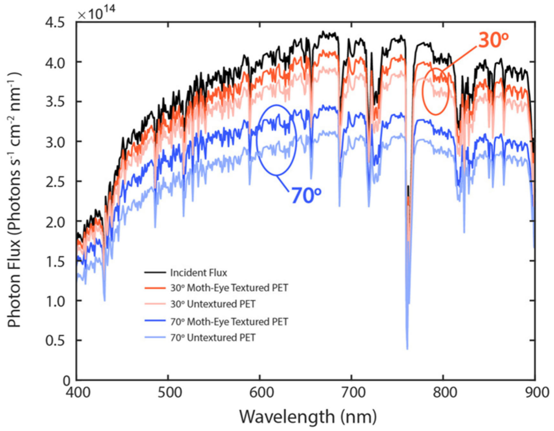

(a)

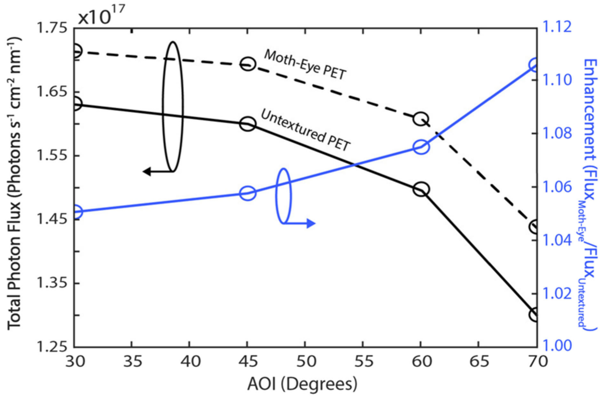

(b)

Fig. 3. (a) Angle-dependent photon flux transmitted through untextured and moth-eye nanotextured PET sheets, calculated using the standard AM1.5D spectrum combined with experimentally measured specular reflectance of moth-eye textured PET sheets at different angles of incidence (darker shade lines) and of an untextured PET sheet (lighter shade lines). The photon flux from the AM1.5D solar spectrum (black line) is shown for reference. (b) Angle dependent photon flux for moth-eye textured and untextured PET films (dashed and solid black lines, respectively) integrated over wavelengths from 400 to 900 nm, and angle-dependent integrated photon flux enhancement through nanotextured PET sheet (blue line).

As shown in Fig. 3, both the moth-eye and nontextured PET sheets transmit fewer photons at increasing AOI due to larger Fresnel reflections. However, compared to the untextured PET, the moth-eye textured PET sheet transmits more photons for all AOI, with a 5% and 10.5% enhancement in transmitted photons at 30° and 70° incidence, respectively. The enhanced omnidirectional performance provided by a moth-eye nanotextured polymer packaging layer would greatly benefit mobile power systems, for example those needed for high altitude pseudo-satellites (HAPS). HAPS systems are generally large, light-weight UAVs where a large fraction of the UAV's surface area is covered in light-weight flexible solar cells for continuous power generation. The curved surface of the UAVs as well as the movement of the sun exposes the solar cells to a large range of AOI which can lead to a loss of power generation efficiency if not managed correctly. Enhanced omnidirectional performance can mitigate efficiency loss due to Fresnel reflections and provide substantial increases in generated power, particularly for illumination at large AOI.

Angle dependent outdoor IV measurements were taken in the early afternoon on a set of cloudless sunny summer days in Austin, TX. Outdoor measurements were performed on both the moth-eye textured PET encapsulated ELO array and a single nontextured PET encapsulated ELO cell. The apparatus and geometry for the angle-dependent measurements are shown schematically in Fig. 4(a). The PV devices are placed on a tip-tilt stage where θ and φ are allowed to vary. The stage is aligned to the sun such that the vector perpendicular to the surface of the PV device is parallel to the impinging sun rays. This position is designated as $\theta = 0°$. Angle dependent IV measurements are performed by varying θ with φ fixed. After successive measurements, the stage is realigned to a new $\theta = 0°$ position to prevent loss of calibration due to the changing position of the sun. Two measurements schemes were used with

Authorized licensed use limited to: University of Texas at Austin. Downloaded on June 25,2021 at 21:27:15 UTC from IEEE Xplore. Restrictions apply.

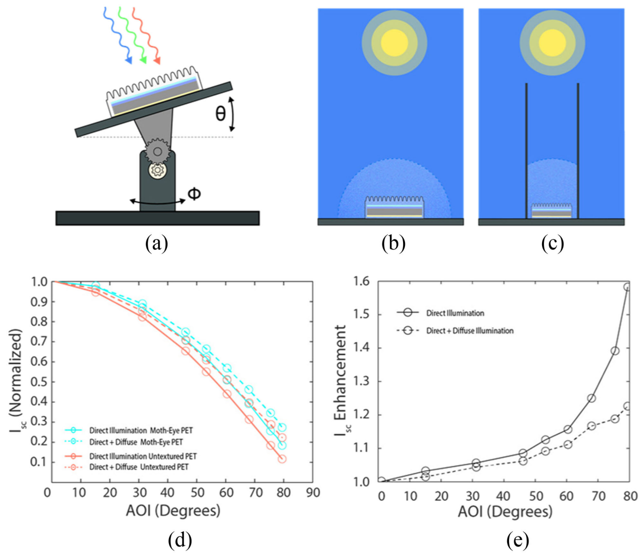

Fig. 4. (a) Schematic of outdoor current–voltage measurement system. System includes motorized stages for accurate azimuthal and altitude alignment. (b) Unobstructed measurement scheme. Diffuse and direct components contribute to power generation. (c) Diffuse excluded measurement scheme. Large confining walls are placed on all sides of the solar cell to prevent the diffuse spectrum from contributing to power generation. (d) Normalized angle dependent I_{sc} measurements for solar cells with laminated moth-eye textured PET packaging (cyan lines) and untextured PET packaging (red lines). I_{sc} measurements under direct illumination (solid lines) and direct + diffuse illumination (dashed lines) are shown. (e) Ratio of normalized angle-dependent I_{sc} measurement for solar cells with laminated moth-eye textured PET packaging to normalized I_{sc} measurement for solar cells with untextured PET packaging under direct (solid line) and direct + diffuse illumination (dashed line).

both PV devices to either exclude or include the diffuse solar illumination. Fig. 4(b) shows a schematic of the PV device placed on the tip-tilt stage without any obstructions. IV measurements performed in this configuration allow a fixed hemisphere of diffuse light to contribute to power generation. The diffuse light is depicted as the light blue circular region surrounding the PV device bounded by the blue dashed line. Fig. 4(c) shows the PV device placed on the tip-tilt stage with large obstructing walls. The obstruction ensures that a smaller volume of diffuse light can reach the PV device and thus allows us to measure PV performance with minimal addition of power generated from the diffuse spectrum. In this arrangement, the bounding volume is $30'' \times 7.5'' \times 7.5''$ and the interior walls are coated with matte-black texturing to prevent successive interior reflections of diffuse light from reaching the PV devices.

Fig. 4(d) shows the angle-dependent I_{sc} of the two solar cell devices under the two different measurement conditions. The measured angle-dependent I_{sc} are normalized to the I_{sc} at normal incidence illumination by

$$\text{Normalized } I_{\mathrm{sc}} = \frac{I_{\mathrm{sc}}\,(\theta)}{I_{\mathrm{sc}}\,(0^{o})} \tag{2}$$

where $I_{\mathrm{sc}}(0°)$ is the short-circuit current measured at normal incidence and $I_{\mathrm{sc}}(\theta)$ is the short-circuit current measured at an AOI of θ. This normalization separates the angular dependence of I_{sc} from the potential cell-to-cell variation in performance. As shown in Fig. 4(d), when solar cells are exposed to direct illumination and the diffuse spectrum is excluded (solid lines), the solar cells encapsulated with nanotextured PET (solid blue line) consistently produce higher I_{sc} values, relative to that at normal incidence, than solar cells encapsulated with untextured PET (solid red line). This is expected since the DLARC antireflection coatings are generally optimized for normal incidence and their antireflection properties become less pronounced at increasing AOI. When directly illuminated, the effective absorbing area of the solar cell decreases quickly for increasing AOI. The omnidirectional current enhancement provided by the moth-eye nanotextured PET sheets can be substantial due to the decrease in effective solar cell area as well as rapidly increasing reflection losses from plane dielectric surfaces as the AOI increases. Fig. 4(e) shows the ratio of the normalized I_{sc} from moth-eye textured solar cells to the normalized I_{sc} from solar cells without nanotexturing under either direct or total (direct + diffuse) solar illumination (solid black line). When considering only direct solar illumination, solar cells encapsulated with moth-eye textured PET produce ~9% and ~58% greater I_{sc} at 46° and 79° AOI, respectively (solid black line), relative to those packaged in untextured PET, when normalized as described above. Similarly, under total solar illumination, solar cells with moth-eye nanotextured PET encapsulating layers produce more short-circuit current than their untextured counterparts for all measured values of $\theta > 0$. This is also expected since moth-eye nanotextured PET sheets are more capable of transmitting incident photons to the solar cell due to their enhanced omnidirectional antireflection properties. Interestingly, Fig. 4(e) shows that the I_{sc} enhancement provided by the moth-eye textured solar cells under total illumination (dashed black line) is significantly lower at large AOI than when under only direct solar illumination. We attribute this to the fact that the effective solar area does not decrease as rapidly under diffuse solar illumination compared to when exposed to only direct solar illumination. This is because as the solar cell is rotated to larger AOI under both direct and diffuse solar illumination, a large fraction of the diffuse hemisphere is still available to be collected by the solar cells regardless of its oblique positioning, while the power in the direct solar spectrum cannot be as easily collected due to the vanishing absorbing surface area. Therefore, the current generated from diffuse illumination becomes a significant fraction of the total current. Since a large fraction of the diffuse hemisphere is still available to solar cells at large AOI, the I_{sc} enhancement is not as pronounced as when only exposed to direct solar illumination. However, as seen in Fig. 4(e), the solar cells under illumination from both direct and diffuse illumination with moth-eye texture PET encapsulant layers (black dashed line) still produce substantially higher I_{sc} than solar cells with untextured PET relative to that at normal incidence, for all angles of incidence $\theta > 0$.

Fig. 5(a) shows the I-V characteristics of the eight ELO cell array with moth-eye nanotextured PET packaging layer at increasing angles of incidence. Fig. 5(b) shows the angle-dependent fill factor and J_{sc} of both the eight ELO cell moth-eye nanotextured array and a single 3J ELO cell without nanotextured PET packaging. Measurements were taken under outdoor direct + diffuse illumination. J_{sc} values of the moth-eye nanotextured array are

Authorized licensed use limited to: University of Texas at Austin. Downloaded on June 25,2021 at 21:27:15 UTC from IEEE Xplore. Restrictions apply.

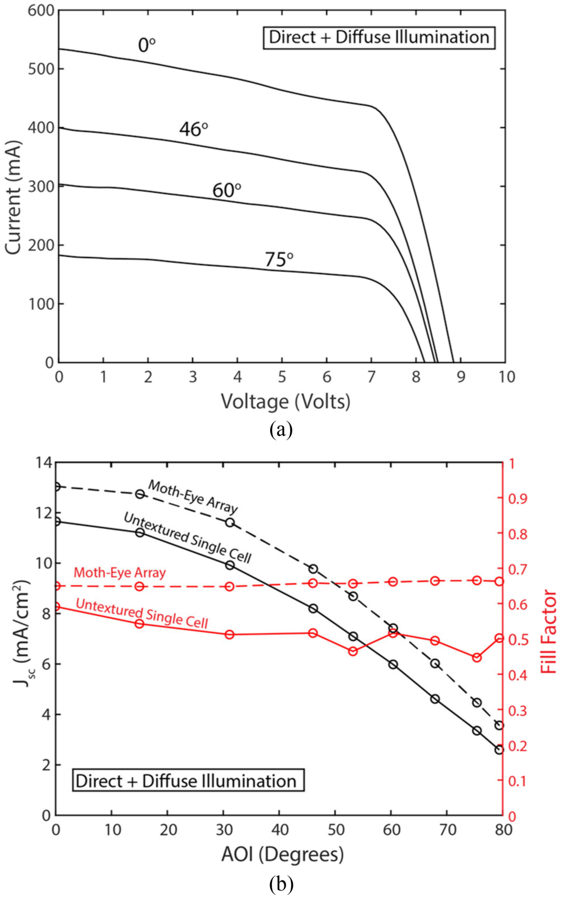

Fig. 5. (a) I-V characteristics of eight cell ELO array with moth-eye nanotextured PET measured at different angles of incidence. I-V measurements were performed under outdoor direct + diffuse illumination. (b) J_{sc} and fill factor measurements at various angles of incidence for eight cell ELO array with moth-eye nanotextured PET packaging and a single ELO solar cell packaged with untextured PET. Measurements were performed under direct + diffuse illumination.

calculated by measuring the I_{sc} of the moth-eye nanotextured array at the respective AOI and dividing by two times the single cell area. Twice the cell area was chosen since the currents in the two parallel branches of four series connected cells are summed at the output of the device. Because the performance characteristics of each cell can vary, any direct comparison in absolute performance between the array and single cell should be interpreted with caution. However, we note that the J_{sc} of the moth-eye nanotextured array is larger than the untextured cell at all AOI due to the increased absorption from diffuse illumination and decrease in reflectance loss. Similarly, the fill factor of the moth-eye nanotextured array is larger at all AOI when compared to the fill factor of the single untextured cell.

In real PV applications, cell efficiency will depend greatly on environmental conditions such as cloudiness and solar positioning. For example, for mobile PV applications such as HAPS systems, the UAVs are constantly exposed to a large range of AOI from mostly direct solar illumination, since the UAVs are flying in the upper atmosphere away from clouds and scattering sources. Therefore, an antireflection surface that can produce more power at larger AOI may provide a substantial boost in total power output. As shown here, solar arrays with moth-eye textured PET packaging that are exposed to direct solar illumination provide current enhancements at all AOI and very large enhancements at large AOI, e.g., ∼58% at 79°. Integrated over the time of flight and the large surface area of the UAV, substantial total energy harvesting enhancements can be expected. Mobile terrestrial applications must additionally mitigate efficiency loss from nonideal cloud cover. Solar cells with integrated PET moth-eye nanostructures have also been shown here to have enhanced current generation from diffuse optical illumination. Therefore, the nanotextured ELO arrays shown in this article may provide substantial efficiency gains and cost reduction for future terrestrial and nonterrestrial applications.

VII. CONCLUSION

In summary, we have demonstrated the integration of moth-eye antireflection nanostructures into a very large area (>200 cm^2) PET polymer packaging sheet. The nanotextured PET sheet was fabricated with a low-cost and scalable NSL technique and was shown to survive commercial lamination procedures to fabricate high-efficiency, lightweight, mechanically flexible, 3J ELO solar arrays. The laminated nanostructures showed minor mechanical degradation due to the lamination procedures but maintained substantial omnidirectional antireflection performance as confirmed by optical characterizations. Outdoor current–voltage measurements were performed on laminated ELO arrays and show that ELO arrays with integrated moth-eye antireflection nanostructures produce more current at all AOI under direct and diffuse solar illumination. Under direct optical illumination moth-eye textured arrays show a maximum I_{sc} enhancement of ∼58% at 79°, and when exposed to both direct and diffuse optical illumination a maximum I_{sc} enhancement of ∼23% at 79° is seen. We anticipate that the low-cost nature of our NSL technique can be leveraged to employ omnidirectional antireflection surfaces for a wide variety of solar applications.

REFERENCES

[1] J. Yoon *et al.*, "Ultrathin silicon solar microcells for semitransparent, mechanically flexible and microconcentrator module designs," *Nat. Mater.*, vol. 7, no. 11, pp. 907–915, Nov. 2008.
[2] H. Jinno *et al.*, "Stretchable and waterproof elastomer-coated organic photovoltaics for washable electronic textile applications," *Nat. Energy*, vol. 2, no. 10, pp. 780–785, Oct. 2017.
[3] S. Zhang and F. Cicoira, "Flexible self-powered biosensors," *Nat.*, vol. 561, pp. 466–467, Sep. 2018.
[4] S. Park *et al.*, "Self-powered ultra-flexible electronics via nano-grating-patterned organic photovoltaics," *Nat.*, vol. 561, no. 7724, pp. 516–521, Sep. 2018.
[5] K. Song *et al.*, "Subdermal flexible solar cell arrays for powering medical electronic implants," *Adv. Healthcare Mater.*, vol. 5, no. 13, pp. 1572–1580, Jul. 2016.
[6] V. R. Voggu *et al.*, "Flexible CuInSe2 nanocrystal solar cells on paper," *ACS Energy Lett.*, vol. 2, no. 3, pp. 574–581, Mar. 2017.
[7] M. C. Barr *et al.*, "Direct monolithic integration of organic photovoltaic circuits on unmodified paper," *Adv. Mater.*, vol. 23, no. 31, pp. 3500–3505, Aug. 2011.
[8] W. Choi *et al.*, "A repeatable epitaxial lift-off process from a single GaAs substrate for low-cost and high-efficiency III-V solar cells," *Adv. Energy Mater.*, vol. 4, no. 16, Nov. 2014, Art. no. 1400589.

Authorized licensed use limited to: University of Texas at Austin. Downloaded on June 25,2021 at 21:27:15 UTC from IEEE Xplore. Restrictions apply.

[9] C. W. Cheng *et al.*, “Epitaxial lift-off process for gallium arsenide substrate reuse and flexible electronics,” *Nat. Commun.*, vol. 4, no. 1, pp. 1–7, Mar. 2013.

[10] R. Tatavarti *et al.*, “Lightweight, low cost GaAs solar cells on 4″ epitaxial liftoff (ELO) wafers,” in *Proc. 33rd IEEE Photovolt. Specialists Conf.*, 2008, pp. 1–4.

[11] G. J. Bauhuis *et al.*, “Wafer reuse for repeated growth of III-V solar cells,” *Prog. Photovolt. Res. Appl.*, vol. 18, no. 3, pp. 155–159, May 2010.

[12] K. M. Trautz *et al.*, “Mobile solar power,” *IEEE J. Photovolt.*, vol. 3, no. 1, pp. 535–541, Jan. 2013.

[13] C. L. Stender *et al.*, “Flexible and lightweight epitaxial lift-off GaAs multi-junction solar cells for portable power and UAV applications,” in *Proc. IEEE 42nd Photovolt. Specialist Conf.*, Dec. 2015, pp. 1–4.

[14] D. Cardwell *et al.*, “Very high specific power ELO solar cells (>3 kW/kg) for UAV, space, and portable power applications,” in *Proc. IEEE 44th Photovolt. Specialist Conf.*, Jun. 2017, pp. 3511–3513.

[15] D. Sato *et al.*, “Design of low-concentration static III-V/Si partial CPV module with 27.3% annual efficiency for car-roof application,” *Prog. Photovolt. Res. Appl.*, vol. 27, no. 6, pp. 501–510, Jun. 2019.

[16] “Giant Solar-Powered UAVs are Atmospheric Satellites – IEEE Spectrum”. Accessed Oct. 15, 2020. [Online]. Available: https://spectrum.ieee.org/automaton/robotics/drones/giant-solar-powered-uavs-are-atmospheric-satellites

[17] “QinetiQ files for three world records for its Zephyr solar powered UAV | Military & Aerospace Electronics”. accessed Oct. 15, 2020. [Online]. Available: https://www.militaryaerospace.com/unmanned/article/16723312/qinetiq-files-for-three-world-records-for-its-zephyr-solar-powered-uav

[18] P. Oettershagen *et al.*, “Perpetual flight with a small solar-powered UAV: Flight results, performance analysis and model validation,” in *Proc. IEEE Aerosp. Conf. Proc.*, Jun. 2016, pp. 1–8.

[19] M. Yamaguchi *et al.*, “Development of high-efficiency and low-cost solar cells for PV-powered vehicles application,” in *Proc. Prog. Photovolt. Res. Appl.*, Sep. 2020, Art. no. 3343.

[20] N. Martin and J. M. Ruiz, “Calculation of the PV modules angular losses under field conditions by means of an analytical model,” *Sol. Energy Mater. Sol. Cells*, vol. 70, no. 1, pp. 25–38, Dec. 2001.

[21] T. Tayagaki, K. Araki, M. Yamaguchi, and T. Sugaya, “Impact of nonplanar panels on photovoltaic power generation in the case of vehicles,” *IEEE J. Photovolt.*, vol. 9, no. 6, pp. 1721–1726, Nov. 2019.

[22] E. Yablonovitch, “Statistical ray optics,” *J. Opt. Soc. Amer.*, vol. 72, no. 7, pp. 899–907, Jul. 1982.

[23] K. J. Yu *et al.*, “Light trapping in ultrathin monocrystalline silicon solar cells,” *Adv. Energy Mater.*, vol. 3, no. 11, pp. 1401–1406, Nov. 2013.

[24] S. M. Lee *et al.*, “High performance ultrathin GaAs solar cells enabled with heterogeneously integrated dielectric periodic nanostructures,” *ACS Nano*, vol. 9, no. 10, pp. 10356–10365, Sep. 2015.

[25] M. L. Brongersma, Y. Cui, and S. Fan, “Light management for photovoltaics using high-index nanostructures,” *Nat. Mater.*, vol. 13, no. 5, pp. 451–460, Apr. 22, 2014.

[26] H. L. Chen *et al.*, “A 19.9%-efficient ultrathin solar cell based on a 205-nm-thick GaAs absorber and a silver nanostructured back mirror,” *Nat. Energy*, vol. 4, no. 9, pp. 761–767, Sep. 2019.

[27] J. Buencuerpo, M. A. Steiner, and A. C. Tamboli, “Optically-thick 300 nm GaAs solar cells using adjacent photonic crystals,” *Opt. Exp.*, vol. 28, no. 9, Apr. 2020, Art. no. 13845.

[28] M. Eerden *et al.*, “A facile light-trapping approach for ultrathin GaAs solar cells using wet chemical etching,” *Prog. Photovolt. Res. Appl.*, vol. 28, no. 3, pp. 200–209, Mar. 2020.

[29] J. Oh, H. C. Yuan, and H. M. Branz, “An 18.2%-efficient black-silicon solar cell achieved through control of carrier recombination in nanostructures,” *Nat. Nanotechnol.*, vol. 7, no. 11, pp. 743–748, Sep. 2012.

[30] X. H. Li, P. C. Li, D. Z. Hu, D. M. Schaadt, and E. T. Yu, “Light trapping in thin-film solar cells via scattering by nanostructured antireflection coatings,” *J. Appl. Phys.*, vol. 114, no. 4, Jul. 2013, Art. no. 044310.

[31] X. Li *et al.*, “Integration of subwavelength optical nanostructures for improved antireflection performance of mechanically flexible GaAs solar cells fabricated by epitaxial lift-off,” *Sol. Energy Mater. Sol. Cells*, vol. 143, pp. 567–572, Dec. 2015.

[32] S. J. Wilson and M. C. Hutley, “The optical properties of ‘moth eye’ antireflection surfaces,” *Opt. Acta*, vol. 29, no. 7, pp. 993–1009, 1982.

[33] D. G. Stavenga, S. Foletti, G. Palasantzas, and K. Arikawa, “Light on the moth-eye corneal nipple array of butterflies,” in *Proc. Biol. Sci.*, vol. 273, pp. 661–667, 2006.

[34] R. H. Siddique, G. Gomard, and H. Hölscher, “The role of random nanostructures for the omnidirectional anti-reflection properties of the glasswing butterfly,” *Nat. Commun.*, vol. 6, no. 1, pp. 1–8, Apr. 2015.

[35] G. Cossio and E. T. Yu, “Zeta potential dependent self-assembly for very large area nanosphere lithography,” *Nano Lett.*, vol. 20, no. 7, pp. 5090–5096, Jul. 2020.

[36] “2000 ASTM Standard Extraterrestrial Spectrum Reference E-490-00 | Grid Modernization | NREL”. Accessed Oct. 07, 2020. [Online]. Available: https://www.nrel.gov/grid/solar-resource/spectra-astm-e490.html

Authorized licensed use limited to: University of Texas at Austin. Downloaded on June 25,2021 at 21:27:15 UTC from IEEE Xplore. Restrictions apply.